9-6-2021

Toward magnetic resonance fingerprinting for low-field MR-guided radiation therapy

Nikolai J. Mickevicius

Joshua Kim
Henry Ford Health, JKIM8@hfhs.org

Jiwei Zhao

Zachary S. Morris

Newton J. Hurst

See next page for additional authors

Delta⁴
by ScandiDos

See us at
ASTRO in booth #1733
Book a meeting with us!

NEW Most advanced Motion Management QA

THE ONLY PLATFORM MOVING IN 7 DIMENSIONS*

We provide medical physicists with a realistic pre-treatment verification of the delivered treatment of moving targets.

In collaboration with Accuray, ScandiDos has developed a solution that improves the quality assurance (QA) of radiotherapy treatments of moving targets. The solution independently simulates the breathing motion of patients, therefore, adding a seventh dimension to the tumor movement simulation provided by the Delta4 HexaMotion. Delta4 motion QA system provides a realistic pre-treatment verification of the delivered treatment for Accuray Radixact® with Synchrony®.

*longitudinal, lateral, height, roll, tilt, time and breathing motion.

Learn more ▶

Delta4family.com

Received: 2 June 2021 | Revised: 17 August 2021 | Accepted: 25 August 2021

DOI: 10.1002/mp.15202

RESEARCH ARTICLE

MEDICAL PHYSICS

Toward magnetic resonance fingerprinting for low-field MR-guided radiation therapy

Nikolai J. Mickevicius[1] | **Joshua P. Kim**[2] | **Jiwei Zhao**[3] | **Zachary S. Morris**[1] | **Newton J. Hurst Jr.**[1] | **Carri K. Glide-Hurst**[1]

[1] Department of Human Oncology, University of Wisconsin-Madison, Madison, Wisconsin, USA

[2] Department of Radiation Oncology, Henry Ford Cancer Institute, Detroit, Michigan, USA

[3] Department of Biostatistics and Medical Informatics, University of Wisconsin-Madison, Madison, Wisconsin, USA

Correspondence
Nikolai J. Mickevicius, PhD, Department of Human Oncology, University of Wisconsin-Madison, 600 Highland Ave, Madison, WI 53792, USA.
Email: nmickevicius@wisc.edu

Funding information
NIH, Grant/Award Number: R01CA204189

Abstract

Purpose: The acquisition of multiparametric quantitative magnetic resonance imaging (qMRI) is becoming increasingly important for functional characterization of cancer prior to- and throughout the course of radiation therapy. The feasibility of a qMRI method known as magnetic resonance fingerprinting (MRF) for rapid T_1 and T_2 mapping was assessed on a low-field MR-linac system.

Methods: A three-dimensional MRF sequence was implemented on a 0.35T MR-guided radiotherapy system. MRF-derived measurements of T_1 and T_2 were compared to those obtained with gold standard single spin echo methods, and the impacts of the radiofrequency field homogeneity and scan times ranging between 6 and 48 min were analyzed by acquiring between 1 and 8 spokes per time point in a standard quantitative system phantom. The short-term repeatability of MRF was assessed over three measurements taken over a 10-h period. To evaluate transferability, MRF measurements were acquired on two additional MR-guided radiotherapy systems. Preliminary human volunteer studies were performed.

Results: The phantom benchmarking studies showed that MRF is capable of mapping T_1 and T_2 values within 8% and 10% of gold standard measures, respectively, at 0.35T. The coefficient of variation of T_1 and T_2 estimates over three repeated scans was $< 5\%$ over a broad range of relaxation times. The T_1 and T_2 times derived using a single-spoke MRF acquisition across three scanners were near unity and mean percent errors in T_1 and T_2 estimates using the same phantom were $< 3\%$. The mean percent differences in T_1 and T_2 as a result of truncating the scan time to 6 min over the large range of relaxation times in the system phantom were 0.65% and 4.05%, respectively.

Conclusions: The technical feasibility and accuracy of MRF on a low-field MR-guided radiation therapy device has been demonstrated. MRF can be used to measure accurate T_1 and T_2 maps in three dimensions from a brief 6-min scan, offering strong potential for efficient and reproducible qMRI for future clinical trials in functional plan adaptation and tumor/normal tissue response assessment.

KEYWORDS
0.35T, low-field, MR fingerprinting, MR-guided radiotherapy, MRF, quantitative imaging, relaxometry

1 | INTRODUCTION

Using multiparametric quantitative magnetic resonance imaging (qMRI) to adapt radiation therapy (RT) plans is a highly sought after frontier in personalized cancer treatment.[1] Efforts are ongoing to acquire quantitative imaging data throughout the course of RT[2–5] and determine the best way to accommodate observed changes in tumor biology in the adaptive RT plan. However, acquiring qMRI data is currently limited by the prohibitively long scan times required to acquire data with sufficient accuracy and spatial resolution. This is especially the case for time-consuming relaxometry (i.e., mapping of the longitudinal and transverse relaxation times T_1 and T_2), which has been shown to correlate with RT treatment response in prostate and brain malignancies.[3,6–8]

To improve the likelihood of patient compliance, innovative methods to minimize qMRI scan time are being developed.[9] One such emerging technique is magnetic resonance fingerprinting (MRF).[10] MRF has emerged as an exciting new method for efficient multiparametric qMRI. Contrary to conventional techniques, MRF acquires data in the transient state by continuously varying pulse sequence parameters like flip angle and repetition time, thereby efficiently encoding differences between qMRI tissue properties into the measured signal at many hundreds to thousands of independent contrast time points. In this manner, each tissue has its own unique MR "fingerprint" that can be matched to a "dictionary" of simulated fingerprints from known tissues. Quantitative parameter maps are then generated through a look-up procedure with the best-matching fingerprint from the dictionary. MRF-derived quantitative measurements of T_1 and T_2 have shown promising clinical use in detecting cancer in the brain,[11] prostate,[12–14] and liver[15] with total scan times near 5 min on 3T MRI scanners. Despite the promise of MRF in diagnostic radiology, however, its use in radiation oncology applications has not been thoroughly investigated.

For radiation oncology applications, preliminary characterizations of MRF have been performed on a dedicated MR-simulator[16 and a] high-field (1.5T) MR-linear accelerator (MR-linac).[17] To-date, however, no studies have been carried out to investigate the feasibility of MRF on low-field (0.35T) MR-linacs, and the feasibility of MRF below 0.55T[18] has not yet been demonstrated. Since T_1 and T_2 times vary with field strength and the signal-to-noise ratio is dramatically lower at low-field,[19] a thorough investigation of the technical feasibility of MRF at 0.35T is required prior to performing large-scale clinical imaging studies. MR-linacs present a unique opportunity to perform longitudinal imaging of cancer patients imaged in the treatment position and open up new potential for acquiring MRF throughout the course of RT.

This study establishes several important technical characteristics of MRF to enable quantitative T_1 and T_2 mapping on a low-field MR-linac system. First, the accuracy of MRF-derived values of T_1 and T_2 was compared to gold standard (GS) methods in a quantitative standardized phantom. The accuracy of MRF as a function of scan time was then studied followed through investigations into the repeatability of MRF and the effects of the transmitting radiofrequency (RF) field homogeneity, including examination of the reproducibility of MRF across three unique MR-linac platforms. Finally, preliminary in vivo MRF experiments were performed on the 0.35T MR-linac. When taken in concert, multiparametric quantitative MRI provides enormous potential to provide actionable information for RT plan adaptation. The validation of MRF at 0.35T is a step toward enabling efficient qMRI-guided RT on low-field MR-linac systems.

2 | MATERIALS AND METHODS

2.1 | MRF implementation

A three-dimensional (3D) gradient spoiled MRF pulse sequence was implemented on a low-field 0.35 T MR-linac (MRIdian Linac, ViewRay, Mountain View, CA). The MRF sequence employed radial *k*-space coverage in-plane and phase-encoded Cartesian coverage along the slice dimension. Radial *k*-space coverage was chosen over the conventional variable density spiral coverage owing to the 0.35T systems being equipped gradient systems capable of producing gradient strengths of only 18 mT/m, which are not strong enough to traverse *k*-space with spiral coverage within the 12 ms repetition time employed in this work. Slab-selective RF pulses with a time-bandwidth product of 10.8 were used for excitation. Between successive RF excitations, the radial spoke rotated by a golden angle of 23.628°.[20] Each repetition of the MRF sequence consisted of nonselective adiabatic inversion preparation followed by a train of $N_{RF} = 512$ gradient echo segments. The flip angle for each of these RF pulses is shown in Figure 1. This pattern was optimized to minimize the theoretical variance in the estimation of T_1 and T_2 using well-established methods.[21] The repetition time (TR) for each of the gradient echo readouts was held constant throughout this study at 12 ms. A delay time of 3 s between MRF repetitions was used to allow for T_1 recovery prior to subsequent inversion pulses.

2.2 | MRF reconstruction

As in Jiang et al.,[22] a dictionary was calculated for this MRF sequence using the extended phase graph formalism[23] with 163 T_1 values between 25 and

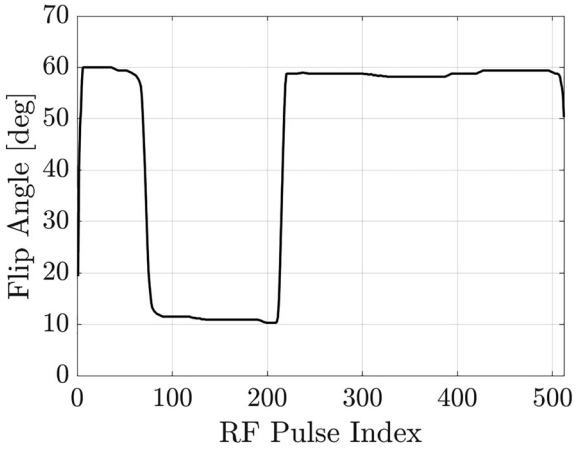

FIGURE 1 Flip angle modulation pattern with 512 radiofrequency (RF) pulse indices used for all magnetic resonance fingerprinting experiments performed in this work

3000 ms in steps of 3%, 204 T_2 values between 5 and 2000 ms in steps of 2%, and 60 B_1^+ scaling factors evenly spaced between 0.3 and 1.2. Tissues with the unlikely combination of $T_2 > T_1$ were omitted.[10,22] A total of 1 324 620 entries were included in the dictionary. To be conservative, the dictionary used here contains approximately 15 times more entries than the B_1^+-corrected approach of Chen et al.,[15] which employs a coarser sampling of T_1, T_2, and B_1^+.

All image reconstructions were performed with a combination of custom Matlab (R2020b, The MathWorks, Natick, MA) and Python code on a laptop with 4-core 2.3 GHz processer and 32 GB RAM. To allow for high acceleration factors, the signal evolution throughout the MRF train of excitation pulses was constrained to span a low-dimensional subspace.[24] The K most dominant basis functions as determined from principal component analysis of the dictionary were used to obtain the subspace $\mathbf{\Phi} \in \mathbb{C}^{N_{RF} \times K}$.[25] In this study, $K = 8$ was heuristically chosen for all reconstructions as this is the threshold at which 90% of the energy of the MRF dictionary is contained. The reconstruction problem posed in Equation (1) was solved for each slice individually with 15 iterations of a linear conjugate gradient algorithm:

$$\min_{\alpha} \|F\mathbf{\Phi}S\alpha - y\|_2^2. \quad (1)$$

Here, $\alpha \in \mathbb{C}^{N \times N \times K}$ is the K-dimensional 2D image to be reconstructed, F is the 2D nonuniform fast Fourier transform operator,[26] S is the RF coil sensitivity map operator, and y is the measured k-space data. The coil sensitivity maps were estimated using the ESPIRiT method.[27] Following reconstruction, a dictionary matching procedure as described in Ma et al. was used to map T_1, T_2, and B_1 in each imaging voxel.[10] Proton density (M_0) was also estimated in arbitrary units (a.u.) as the ratio of the ℓ_2-norm of the measured signal evolution in a voxel to that of the matching dictionary entry. The total processing time for each 3D MRF dataset was approximately 30 min.

2.3 | MRF benchmarking data acquisition

Benchmarking coronal MRF data were acquired in scanner A in the NIST/ISMRM System Standard Model 130 Phantom (S/N 130-0130, QalibreMD, Boulder, CO) at a spatial resolution of 1.64 x 1.64 x 5 mm^3 and a matrix size of 128 x 128 x 32. To investigate the impact of undersampling k-space, a large dataset consisting of eight unique radial spokes per point in the MRF pattern was acquired. The angle of each of these spokes was defined by the golden angle increment of $\theta = 111.246° \cdot n$ where $n \in [1, 2, \ldots 8]$.[28] This resulted in a total MRF scan time of about 48 min. To investigate the impact of reducing MRF scan time on the estimated values of T_1 and T_2, MRF reconstructions were performed using all available data and for retrospectively undersampled datasets with 1, 2, 3, and 5 spokes per frame, which corresponded to scan times of 6, 12, 18, and 30 min, respectively. The number of spokes in each of these retrospectively undersampled MRF datasets was chosen to be a Fibonacci number to ensure approximately uniform azimuthal k-space coverage using the golden angle increment.[28] An actual flip angle imaging (AFI) sequence[29] was acquired to externally map B_1^+ at a resolution of 4.92 x 4.92 x 5 mm^3 with a flip angle of 45°, TR_1 of 20 ms, TR_2 of 100 ms, and total scan time of 4 min. GS T_1 and T_2 maps were acquired in the NIST/ISMRM phantom[30] with approximately 10 h of scan time using the parameters of a 2D spin echo pulse sequence shown in Table 1. The field-of-view and spatial resolution matched that of the MRF scans. Temperature was monitored within the phantom to ensure reliability and the difference was less than 0.3°C over the entire experiment.

2.3.1 | Analysis 1: comparison of MRF and GS T_1 and T_2 times

Within circular regions of interest (ROIs) with radii of four pixels (6.56 mm), the mean T_1 and T_2 times within the spheres in the T_1 and T_2 plates of the NIST/ISMRM phantom were calculated for the GS and full (i.e., 8 spokes per frame) MRF measurements. The ROIs were small enough to be fully contained within the cross section of the phantom spheres to mitigate any potential partial volume effects. This was done for three B_1^+ compensation approaches: (1) fitting for T_1 and T_2 using an externally calibrated B_1^+ map[15] from the AFI scan, (2) fitting for T_1, T_2, and B_1^+ simultaneously using

TABLE 1 Scan parameters of a 2D spin echo pulse sequence for GS T_1 and T_2 mapping

	Inversion time [ms]	Echo time [ms]	TR [ms]
GS T_1 mapping	23, 100, 200, 400, 800, 1600, and 3200	12	10 000
GS T_2 mapping	N/A	12, 22, 42, 62, 102, 152, and 202	10 000

the MRF dictionary,[31] and (3) ignoring B_1^+ variations.[22] These three approaches were used to determine if the externally mapped B_1^+ compensation and the dictionary-compensated B_1^+ approaches yielded similar T_1 and T_2 times, thus making the separate AFI acquisition unnecessary, which has implications for throughput and efficiency. Regression analyses were performed to characterize the performance of MRF relative to GS methods for each of the B_1^+ compensation approaches. Following Kolmogorov–Smirnov (KS) tests for normality, paired *t*-tests were used to compare the T_1 and T_2 times from each MRF dataset to those estimated using the GS methods.

2.3.2 | Analysis 2: comparison of full MRF and accelerated MRF T_1 and T_2 times

The retrospectively undersampled phantom MRF datasets were used to assess the impact of MRF scan duration on calculated T_1 and T_2 times. Within the spheres in the T_1 and T_2 plates of the NIST/ISMRM phantom, the mean T_1 and T_2 times were calculated for reconstructions from 1, 2, 3, 5, and 8 radial *k*-space spokes per frame. Regression and Bland–Altman analyses were performed using Matlab for quantitative comparison between relaxation times derived from varying MRF scan durations. Mean percent differences were calculated for the accelerated T_1 and T_2 measurements compared to the fully sampled measurements. Once normality was confirmed via KS testing, paired *t*-tests were also used to test for significant differences between the accelerated and 8-spoke MRF T_1 and T_2 times in Matlab.

2.3.3 | Analysis 3: short-term repeatability of MRF

The repeatability of T_1 and T_2 times derived using MRF was assessed in three single-spoke-per-frame datasets. The first two datasets were acquired within 12 min of each other, while the third dataset was acquired after completion of the 10 h of GS data acquisition. The coefficient of variation, calculated as the ratio of the standard deviation to the mean, over these three measurements was calculated as a function of mean T_1 and T_2 times. The repeatability coefficient (RC), as described by Barnhart and Barboriak,[32] was calculated for T_1 and T_2 over the three measurements. The interpretation of the RC here is that the difference in T_1 or T_2 between any two of the serial measurements in the same phantom vial is expected to be within –RC to +RC for 95% of all of the vials.

2.3.4 | Analysis 4: interscanner reproducibility of MRF

Using identical scan protocols for the phantom experiment as those shown above, an NIST/ISMRM system phantom with Serial Number 0088 was scanned three times on two additional 0.35T MR-Linac systems (scanners B and C). The mean percent difference in T_1 and T_2 times calculated between scanners B and C was calculated where the same phantom was used on both systems. Using the R language,[33] the intraclass correlation coefficient (ICC) was used to assess the consistency of the three repeated measures of T_1 and T_2 measurements made between all three scanners.[34,35] Separately for T_1 and T_2, a Kruskal–Wallis one-way analysis of variance was also used to test if the differences between the relaxation time measurements from the three scanners were statistically significant.[36,37] Mean relaxation times were estimated within fixed ROI sizes between scanners.

2.3.5 | Analysis 5: in vivo MRF

MRF data in the pelvis, thigh, brain, and head/neck were acquired as part of an institutional review board-approved healthy volunteer study. Common parameters for all in vivo scans include a matrix size of 256 x 256 x 32, readout bandwidth of 200 Hz/pixel, slice thickness of 3 mm, and 25% slice oversampling. Based on the results of the phantom experiments shown below, the in vivo MRF datasets were acquired with a single-spoke per contrast point in 6 min of scan time. The in-plane fields-of-view for the pelvis, thigh, brain, and head/neck acquisitions were 360, 300, 300, and 350 mm, respectively. Qualitative evaluation was conducted of the presence and severity of artifacts in the MRF data. In the brain MRF dataset, the mean and standard deviation of T_1 and T_2 times from an 8x8 pixel region in frontal white matter were calculated for comparison with published values at 0.35T.

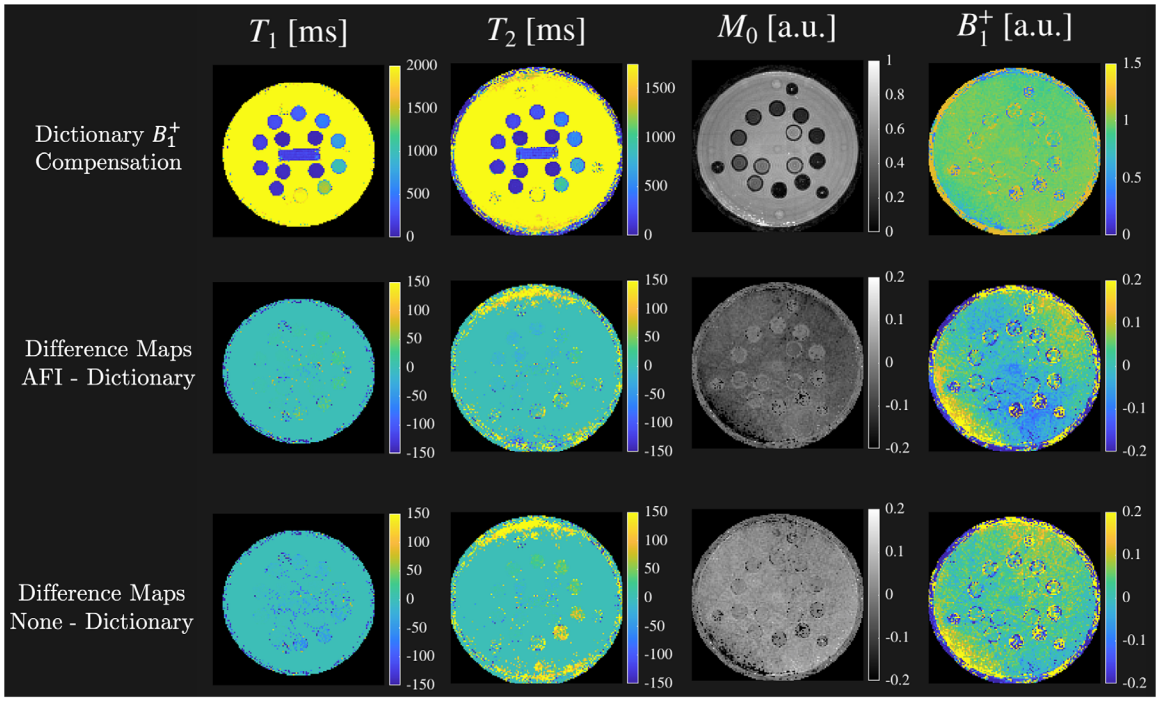

FIGURE 2 (Top row) T_1, T_2, and proton density (M_0) maps shown in their respective slices of the NIST/ISMRM system phantom using the 8 spokes per frame magnetic resonance fingerprinting (MRF) dataset on a 0.35T MR-linac. The top row was generated using a dictionary matching procedure that included the mapping of B_1^+ (top right). Differences between each quantitative map for the actual flip angle imaging (AFI) compensated reconstruction and ignoring B_1^+ variations can be seen in the middle and bottom rows, respectively. The B_1^+ maps are shown in the same plate as the T_2 maps

3 | RESULTS

3.1 | Analysis 1 results: MRF versus GS

For qualitative comparison, the T_1, T_2, proton density (M_0), and B_1^+ maps from the 8-spoke MRF reconstruction in the system phantom can be seen in Figure 2 for the dictionary B_1^+-compensated approach. The difference maps shown in Figure 2 highlight that while the differences in T_1 maps between the B_1^+ compensation approaches are minimal, larger deviations can be observed in T_2 maps in spheres with longer T_2 times, particularly when ignoring B_1^+ variations as evidenced by the larger differences in T_2 (Figure 2, bottom).

Figure 3 better quantifies the impact of the MRF approaches on T_1 and T_2 values as compared with GS methods. The linear equations of best fit of MRF-derived values of T_1 and T_2 compared with those derived with GS methods can be seen in Figures 3a and b, respectively. The R^2 values from the linear fits were greater than or equal to 0.998 in each case. Bland–Altman plots in Figures 3c and d show the difference between MRF and GS T_1 and T_2 values as a function of mean GS value. The differences between all mean MRF and GS T_1 and T_2 values were found to lie on a normal distribution from the KS test for normality ($p > 0.05$). With all approaches, MRF underestimates T_1 (6.3% for AFI-mapped B_1^+ [$p = 0.002$], 8.2% for dictionary-mapped B_1^+ [$p = 0.001$], and 9.7% for ignored B_1^+ [$p = 0.002$]) and T_2 (18.6% for AFI-mapped B_1^+ [$p = 0.005$], 10.0% for dictionary-mapped

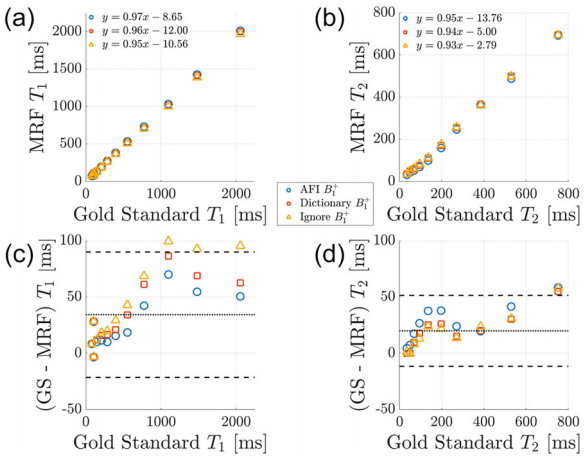

FIGURE 3 Mean MRF-derived T_1 and T_2 values versus mean GS T_1 and T_2 times derived using inversion recovery spin echo and multiecho spin echo imaging, respectively, in the NIST/ISMRM phantom. These MRF values were obtained using the full 48-min (8 spokes) dataset. The R^2 values from the linear fits were greater than or equal to 0.998 in each case. The Bland–Altman plots below show the bias and 95% confidence interval for the difference between the GS and MRF measurements

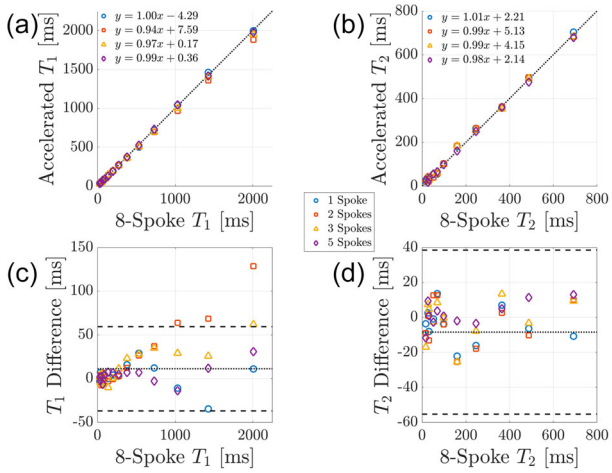

FIGURE 4 Comparison of MRF-derived measures of T_1 and T_2 for truncated MRF datasets with 1, 2, 3, and 5 spokes per frame compared with the full 8 spokes per frame. Plots (a) and (b) show the agreement between the accelerated and full MRF scans, while (c) and (d) show the relaxation time-dependent differences. The R^2 values from the linear fits were greater than or equal to 0.997 in each case. The Bland–Altman plots below show the bias and 95% confidence interval for the difference between the 48-min and accelerated MRF measurements

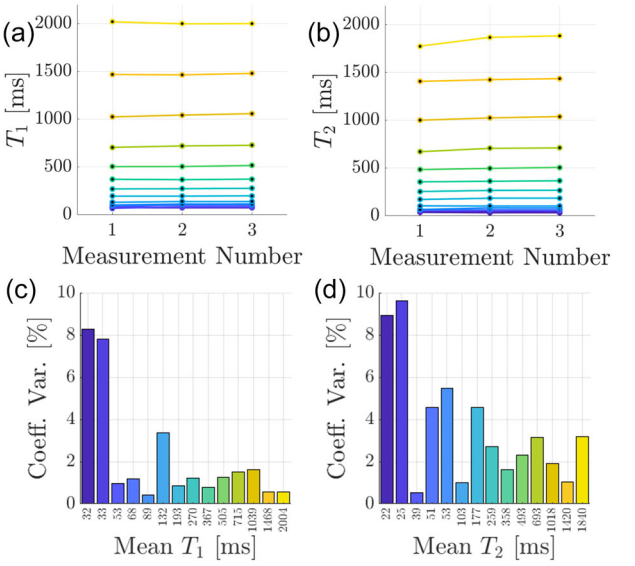

FIGURE 5 Short-term repeatability results for MRF-derived values of T_1 and T_2 at 0.35T. Measurements 1 and 2 were acquired within a 12-min period, while measurement 3 was acquired approximately 10 h later. In (a) and (b), the mean T_1 and T_2 times are plotted across the three measurements with each line belonging to one sphere of the system phantom. The coefficients of variation (Coeff. Var.) across the three timepoints for T_1 and T_2 are shown in (c) and (d), respectively. The color of each line in (a) and (b) corresponds to the mean T_1 and T_2 times in (c) and (d)

B_1^+ [$p = 0.003$], and 9.22% for ignored B_1^+ [$p = 0.006$]). Mapping B_1^+ with the dictionary matching procedure improved the mean percent error in the estimation of T_2 by 8.6% compared with the AFI-mapped B_1^+ compensation.

3.2 | Analysis 2 results: scan time comparison

The quantitative impact of retrospectively undersampling the 8-spoke MRF dataset to 1, 2, 3, and 5 spokes can be seen in Figure 4. The equations of best fit of the mean T_1 and T_2 times of the accelerated MRF datasets to those of the full 8-spoke dataset are shown in Figures 4a and b. The R^2 values from the linear fits were greater than or equal to 0.997 in each case. For both T_1 and T_2, small errors were observed (mean percent errors of 0.65% and 4.05%, respectively) between the single-spoke and full datasets. For very short T_1 times less than 250 ms, the error due to using a shorter scan time was less than 10 ms. The error for T_1 times greater than 250 ms increases with increasing T_1 time, with the largest deviations observed for the 2-spoke MRF dataset. The 1- and 5-spoke reconstructions performed similarly well in terms of T_1 accuracy. The T_2 values from all undersampled MRF datasets were close to those from the full 8-spoke dataset as seen with the slopes of the lines of best fit near 1.0 and small differences across the full 700 ms range in the Bland–Altman plot in Figure 4d. The differences between the T_1 and T_2 times estimated from the accelerated MRF datasets and those from the full 8-spoke datasets were found to lie on a normal distribution (KS test p-value > 0.05) and were not significantly different (t-test p-value > 0.05 in all cases).

3.3 | Analysis 3 results: repeatability

The mean values of T_1 and T_2 within the NIST/ISMRM system phantom over three separate single-spoke MRF measurements (sequential and then 10 h after) can be seen in Figures 5a and b, respectively. The coefficient of variation for T_1 and T_2 times for each sphere in the phantom is shown in Figures 5c and d. Except for T_1 times smaller than 35 ms, which are unlikely to be encountered in vivo, the coefficient of variation in T_1 times was less than 4%. The coefficients of variation in T_2 estimates made over the three MRF measurements were larger than those for T_1, but still were near or under 5% for T_2 times greater than 30 ms. The RC values for T_1 and T_2 were calculated to be 21.6 and 51.5 ms, respectively.

3.4 | Analysis 4 results: reproducibility

The results of the reproducibility experiments can be seen in Figure 6. Scanner A served as a reference for measurements made from scanners B and C as

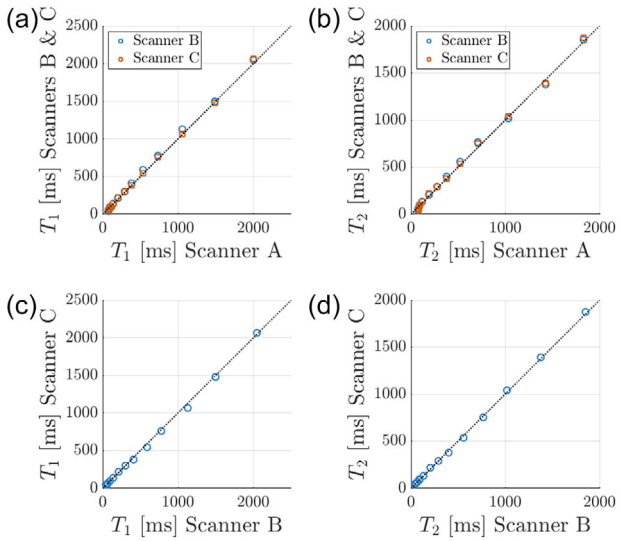

FIGURE 6 Reproducibility of MRF at 0.35T. (a) and (b) demonstrate the strong agreement between T_1 and T_2 values acquired at two different institutions, while (c) and (d) highlight the agreement using the same phantom on two different MR-linacs at the same institution

it was used for all benchmarking experiments shown above. The mean percent error between T_1 and T_2 estimates made between scanners B and C was 2.92% and 2.71%, respectively. For both T_1 and T_2, the ICC was found to be equal to 1, with the 95% confidence interval for the ICC being [1,1]. No significant differences were observed in the Kruskal–Wallis tests between scanners (A, B, and C, with two different ISMRM/NIST phantoms) for both T_1 and T_2 ($p = 0.99$ and $p = 0.98$, respectively). When the same phantom was used for scanners B and C, no statistically significant differences were found for both T_1 and T_2 ($p = 0.89$ and $p = 0.93$, respectively).

3.5 | Analysis 5 results: in vivo MRF

Quantitative in vivo T_1 and T_2 maps derived from MRF data acquired in 6 min for the pelvis and thigh MRF datasets are shown in Figure 7. As expected within the prostate in the pelvic MRF datasets,[38] longer mean T_1 and T_2 times in the peripheral zone (2024.9 and 576.3 ms, respectively) were observed relative to those from the central gland (790.2 and 150.2 ms, respectively). The T_2 maps in both the pelvic and thigh datasets appear noisier than the T_1 maps, which is consistent with other MRF implementations.[39] The quantitative parameter maps, however, do not contain radial streaking artifacts even though only a single radial *k*-space spoke was acquired at each point in the MRF flip angle pattern. The B_1^+ scaling factors are near unity (0.99 ± 0.19 a.u.) over the entire pelvic field-of-view, which is expected given the reduced dielectric effect at 0.35T compared to high field diagnostic systems.[19]

MRF-derived measures of T_1, T_2, and proton density in the brain and head/neck are shown in Figure 8. Two axial slices of the brain data are shown, and the natively acquired axial images are shown for the head/neck dataset along with a reformatted sagittal view. The sagittal view demonstrates the ability of MRF to generate T_1 and T_2 maps throughout the entire prescribed 3D volume. In the brain, the mean and standard deviations of frontal white matter T_1 and T_2 times were observed to be 433.1 ± 15.2 ms and 55.5 ± 5.3 ms, respectively. In the axial plane, the T_1 and T_2 maps from the head and neck dataset do not contain radial streaking artifacts and exhibit similar image quality to the other anatomical sites. The sagittal reformat of the head and neck T_1 and T_2 maps demonstrates the capability of MRF to map relaxation times with high quality throughout all measured slices.

4 | DISCUSSION

To our knowledge, this work is the first to report the potential utility of MRF at a low-field strength (0.35T) with the overarching goal of supporting using MRF for multiparametric quantitative imaging biomarker studies in MR-guided radiotherapy. It was shown that the 3D MRF implementation made at 0.35T produced T_1 and T_2 values from a 6-min scan that were highly correlated with those derived using GS spin echo methods. Similar to the work of Assländer et al.,[40] this rapid scan time was achieved by acquiring a single radial *k*-space spoke per point in the MRF pattern for each phase-encoded 3D partition. A minor underestimation of T_1 and T_2 values was observed, though this is consistent with other MRF validation studies.[10,22,41] In Figure 3, the Bland–Altman plots appear to show a dependence of the difference in MRF- and GS-derived T_1 and T_2 estimates on mean T_1 and T_2 times. At small T_1 and T_2 times, MRF underestimates relaxation times, and the differences vary slowly as relaxation times increase. A similar result can be seen in Jiang et al.[42] Further, with the coefficients of variation over several measurements near or below 5%, it was demonstrated that MRF-derived T_1 and T_2 values are repeatable over a wide range of relaxation times. The in vivo MRF-derived T_1 and T_2 maps produced measurements were devoid of streaking artifacts despite the extreme undersampling of *k*-space performed herein.

It was expected that measuring B_1^+ using the well-established AFI method and incorporating this information into the MRF reconstruction would improve the accuracy of both T_1 and T_2 estimates. However, with respect to GS methods, MRF-based T_1 mapping was most accurate when incorporating the B_1^+ map calculated with AFI, but the accuracy in T_2 was

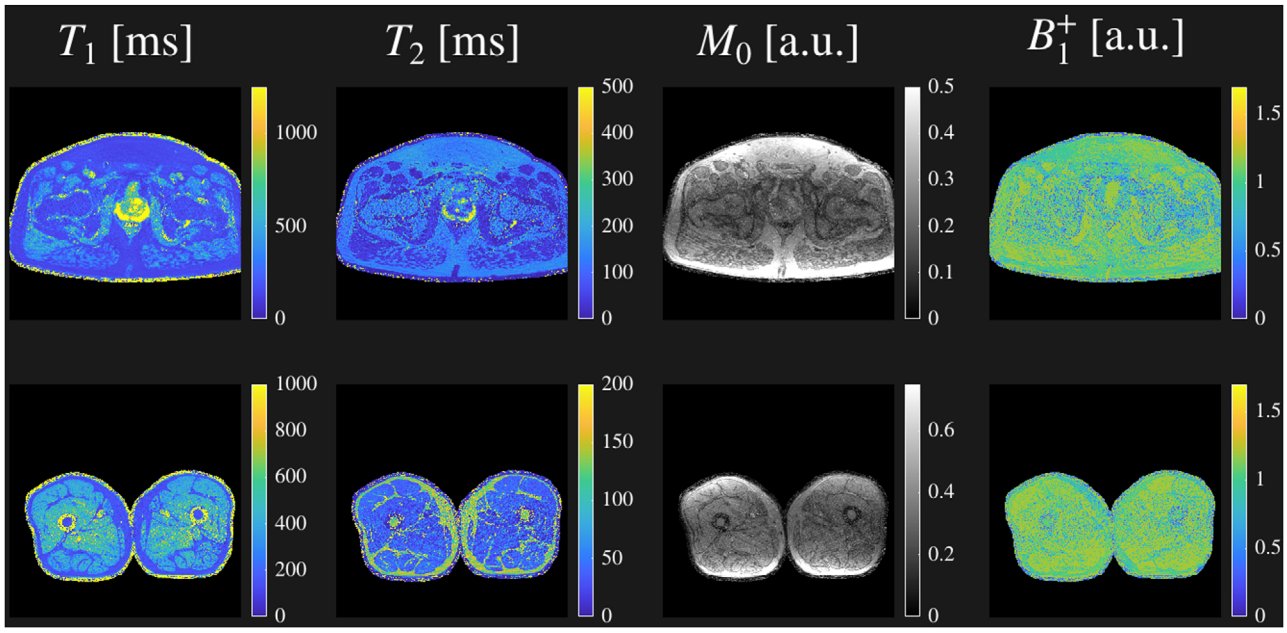

FIGURE 7 In vivo MR fingerprinting results at 0.35T in the pelvis (top row) and thigh (bottom row) of a healthy male volunteer. Quantitative T_1 and T_2 maps are shown along with the quantitative B_1^+ scaling factor and semiquantitative proton density (M_0)

worst when incorporating the externally measured B_1^+ map. Confounding effects that may have contributed to errors in the AFI B_1^+ maps could include insufficient gradient spoiling[43] and lack of an optimized selection of the flip angle and repetition times.[44] Nevertheless, the use of the dictionary-based mapping of T_1, T_2, and B_1^+ provided T_1 and T_2 estimates that were near 8% and 10% of GS measurements, respectively, and we were still able to confirm our hypothesis that a separate AFI scan is not required to obtain accurate quantitative T_1 and T_2 maps using MRF at 0.35T.

Overall, excellent reproducibility of MRF at 0.35T was observed via phantom experiments conducted on three low-field MR-linac systems. The MRF-derived measurements of T_1 and T_2 made between three scanners from two institutions were found to be highly reproducible, as determined by very strong ICC values. Further, no statistically significant differences were observed between the distribution of the T_1 and T_2 measurements between scanners, regardless of whether the same phantom was used. Using the same phantom for scanners B and C allowed a direct mean percent error comparison of T_1 and T_2 times in the phantom that were calculated to be $< 3\%$. This supports the implementation of MRF at 0.35T to yield reproducible estimates of T_1 and T_2, suggesting promise for future multi-institutional quantitative imaging biomarker studies using MR-linacs. Recent work has also highlighted the high degree of repeatability and reproducibility of MRF-based measurements of T_1 and T_2 at field strengths of 1.5T and 3T between three international centers.[41]

In vivo, the observed T_1 and T_2 values from the MRF dataset in frontal white matter of 433.1 and 55.5 ms, respectively, were comparable to the T_1 (390–414 ms) and T_2 (54.3 ms) times available in the literature at 0.35T.[3,45] The elongated T_1 and T_2 times in the peripheral zone of the prostate relative to those within the central gland as observed by MRF here at 0.35T are not directly comparable to those observed at high field, but they exhibit a similar magnitude of difference between these areas of the prostate as those measured at 3T[12] (i.e., approximately two to three times longer T_1 values and three to four times longer T_2 values). While published T_1 and T_2 times are not readily available for direct comparison within the other body sites evaluated (i.e., thigh for soft tissue sarcoma and head and neck), the overall quality of the in vivo MRF datasets was comparable to previously published methods at higher field strengths, despite being performed at the low-field strength of 0.35T.

There are a few limitations of this implementation of MRF at 0.35T. First, a relatively low readout bandwidth between 150 and 200 Hz/pixel was used to compensate for the poor signal-to-noise ratio at the low magnetic field strength. This could result in blurring of the quantitative maps if areas of severe magnetic field homogeneity are encountered.[46] Further, water and fat partial volume effects could have led to a bias in the in vivo relaxation maps.[47] A water-fat separated MRF implementation could minimize these biases.[48] Other confounding effects, such as diffusion and magnetization transfer, were also not considered here but can be explored in future work.

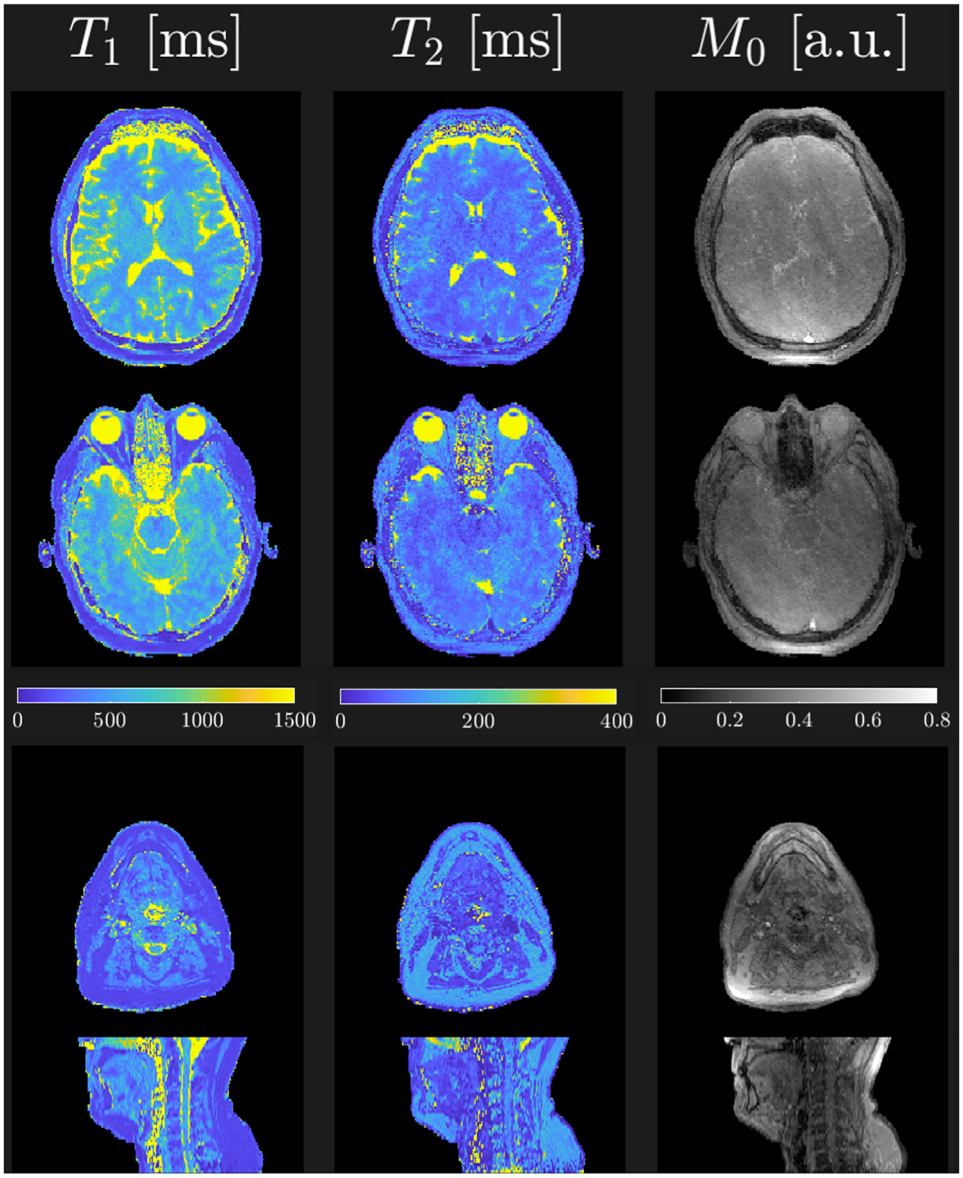

FIGURE 8 MR fingerprinting maps of T_1, T_2, and proton density (M_0) in the brain and head/neck volunteer studies on a 0.35T MR-guided radiation therapy system. Two axial slices are shown in the brain (top), while a single axial slice and a sagittal reformatted image are shown in the head/neck dataset (bottom)

Compared with previously published MRF studies,[31,49] this approach employed a relatively large dictionary to eliminate the possibility of a coarse dictionary resolution biasing the results. Future studies will seek an optimal balance between dictionary resolution, quantitative parameter accuracy, and computation time in the context of low-field MR-guided RT. An approach like Roeloffs et al. in which small dictionaries are used in conjunction with an interpolation of the Bloch-response manifold to map tissue parameters with arbitrary resolution may be explored.[50]

Future work may explore the use of more advanced MRF reconstruction algorithms employing data-driven regularization and dictionary-free parameter mapping to allow the boundaries of scan time acceleration to be pushed in support of rapid acquisition during MR-guided RT treatments. Finally, with further motion robustness strategies, extensions toward other body sites such as abdomen will be pursued in future work.

5 | CONCLUSIONS

This feasibility study on MR fingerprinting at 0.35T demonstrated the promising potential for the rapid acquisition of T_1 and T_2 maps on low-field MR-guided RT systems. Like the work of Bruijnen et al. demonstrating the feasibility of MRF on a high-field MR-Linac,[17]

this work at low-field opens the door for future investigations into the characterization of tumors for outcome prediction, response assessment, and the exploratory use of MRF for qMRI-based dose plan adaptation with efficiently acquired multiparametric quantitative imaging.

ACKNOWLEDGMENTS

The authors thank the generous support of this work from the Bentson Foundation and the University of Wisconsin Bentson Translational Research Fellowship.

CONFLICTS OF INTEREST

The authors have no conflicts of interest to disclose.

DATA AVAILABILITY STATEMENT

The data supporting the results of this study are available upon reasonable request to the corresponding author.

REFERENCES

1. van Houdt PJ, Yang Y, van der Heide UA. Quantitative magnetic resonance imaging for biological image-guided adaptive radiotherapy. *Front Oncol*. 2021;10:615643, https://doi.org/10.3389/fonc.2020.615643
2. Yang Y, Cao M, Sheng K, et al. Longitudinal diffusion MRI for treatment response assessment: preliminary experience using an MRI-guided tri-cobalt 60 radiotherapy system. *Med Phys*. 2016;43(3):1369-1373.
3. Nejad-Davarani SP, Zakariaei N, Chen Y, et al. Rapid multicontrast brain imaging on a 0.35T MR-linac. *Med Phys*. 2020;47(9):4064-4076.
4. Gao Y, Kalbasi A, Hsu W, et al. Treatment effect prediction for sarcoma patients treated with preoperative radiotherapy using radiomics features from longitudinal diffusion-weighted MRIs. *Phys Med Biol*. 2020;65(17):175006.
5. Simpson G, Spieler B, Dogan N, et al. Predictive value of 0.35 T magnetic resonance imaging radiomic features in stereotactic ablative body radiotherapy of pancreatic cancer: a pilot study. *Med Phys*. 2020;47(8):3682-3690.
6. Foltz WD, Wu A, Chung P, et al. Changes in apparent diffusion coefficient and T_2 relaxation during radiotherapy for prostate cancer. *J Magn Reson Imaging*. 2013;37(4):909-916.
7. van Schie MA, van Houdt PJ, Ghobadi G, et al. Quantitative MRI changes during weekly ultra-hypofractionated prostate cancer radiotherapy with integrated boost. *Front Oncol*. 2019;9:1264.
8. Chan RW, Chen H, Myrehaug S, et al. Quantitative CEST and MT at 1.5T for monitoring treatment response in glioblastoma: early and late tumor progression during chemoradiation. *J Neurooncol*. 2020;151(2):267-278.
9. Deoni SCL, Rutt BK, Peters TM. Rapid combined T_1 and T_2 mapping using gradient recalled acquisition in the steady state. *Magn Reson Med*. 2003;49(3):515-526.
10. Ma D, Gulani V, Seiberlich N, et al. Magnetic resonance fingerprinting. *Nature*. 2013;495(7440):187-192.
11. Badve C, Yu A, Dastmalchian S, et al. MR fingerprinting of adult brain tumors: initial experience. *AJNR Am J Neuroradiol*. 2017;38(3):492–499.
12. Yu AC, Badve C, Ponsky LE, et al. Development of a combined MR fingerprinting and diffusion examination for prostate cancer. *Radiology*. 2017;283(3):729-738.
13. Panda A, Obmann VC, Lo W-C, et al. MR fingerprinting and ADC mapping for characterization of lesions in the transition zone of the prostate gland. *Radiology*. 2019;292(3):685-694.
14. Panda A, O'connor G, Lo WC, et al. Targeted biopsy validation of peripheral zone prostate cancer characterization with magnetic resonance fingerprinting and diffusion mapping. *Invest Radiol*. 2019;54(8):485-493.
15. Chen Y, Jiang Y, Pahwa S, et al. MR fingerprinting for rapid quantitative abdominal imaging. *Radiology*. 2016;279(1):278-286.
16. Lu L, Chen Y, Shen C, et al. Initial assessment of 3D magnetic resonance fingerprinting (MRF) towards quantitative brain imaging for radiation therapy. *Med Phys*. 2020;47(3):1199-1214.
17. Bruijnen T, Van Der Heide O, Intven MPW, et al. Technical feasibility of magnetic resonance fingerprinting on a 1.5T MRI-linac. *Phys Med Biol*. 2020;65(22):22-23.
18. Campbell-Washburn AE, Jiang Y, Körzdörfer G, Nittka M, Griswold MA. Feasibility of MR fingerprinting using a high-performance 0.55 T MRI system. *Magn Reson Imaging*. 2021;81:88-93.
19. Marques JP, Simonis FFJ, Webb AG. Low-field MRI: an MR physics perspective. *J Magn Reson Imaging*. 2019;49(6):1528-1542.
20. Wundrak S, Paul J, Ulrici J, et al. Golden ratio sparse MRI using tiny golden angles. *Magn Reson Med*. 2016;75(6):2372-2378.
21. Zhao B, Haldar JP, Liao C, et al. Optimal experiment design for magnetic resonance fingerprinting: Cramér-Rao bound meets spin dynamics. *IEEE Trans Med Imaging*. 2019;38(3):844-861.
22. Jiang Y, Ma D, Seiberlich N, Gulani V, Griswold MA. MR fingerprinting using fast imaging with steady state precession (FISP) with spiral readout. *Magn Reson Med*. 2015;74(6):1621-1631.
23. Weigel M. Extended phase graphs: dephasing, RF pulses, and echoes — pure and simple. *J Magn Reson Imaging*. 2015;41(2):266-295.
24. Zhao B, Setsompop K, Adalsteinsson E, et al. Improved magnetic resonance fingerprinting reconstruction with low-rank and subspace modeling. *Magn Reson Med*. 2018;79(2):933-942.
25. Tamir JI, Uecker M, Chen W, et al. T_2 shuffling: sharp, multicontrast, volumetric fast spin-echo imaging. *Magn Reson Med*. 2017;77(1):180-195.
26. Fessler JA, Sutton BP. Nonuniform fast Fourier transforms using min-max interpolation. *IEEE Trans Signal Process*. 2003;51(2):560-574.
27. Uecker M, Lai P, Murphy MJ, et al. ESPIRiT—an eigenvalue approach to autocalibrating parallel MRI: where SENSE meets GRAPPA. *Magn Reson Med*. 2014;71(3):990-1001.
28. Winkelmann S, Schaeffter T, Koehler T, Eggers H, Doessel O. An optimal radial profile order based on the golden ratio for time-resolved MRI. *IEEE Trans Med Imaging*. 2007;26(1):68-76.
29. Yarnykh VL. Actual flip-angle imaging in the pulsed steady state: a method for rapid three-dimensional mapping of the transmitted radiofrequency field. *Magn Reson Med*. 2007;57(1):192-200.
30. Stupic KF, Ainslie M, Boss MA, et al. A standard system phantom for magnetic resonance imaging. *Magn Reson Med*. 2021;86:1194-1211.
31. Buonincontri G, Sawiak SJ. MR fingerprinting with simultaneous B_1 estimation. *Magn Reson Med*. 2016;76(4):1127-1135.
32. Barnhart HX, Barboriak DP. Applications of the repeatability of quantitative imaging biomarkers: a review of statistical analysis of repeat data sets. *Transl Oncol*. 2009;2(4):231-235.
33. R Core Team R: A Language and Environment for Statistical Computing. 2013. http://www.r-project.org/, last accessed August 9th, 2021
34. Shrout PE, Fleiss JL. Intraclass correlations: uses in assessing rater reliability. *Psychol Bull*. 1979;86(2):420-428.
35. Koo TK, Li MY. A guideline of selecting and reporting intraclass correlation coefficients for reliability research. *J Chiropr Med*. 2016;15(2):155.
36. Kruskal WH, Wallis WA. Use of ranks in one-criterion variance analysis. *J Am Stat Assoc*. 1952;47(260):583-621.
37. Corder GW, Foreman DI. *Nonparametric Statistics for Non-Statisticians*. A Step-by-Step Approach. 2011.

38. Liney GP, Knowles AJ, Manton DJ, Turnbull LW, Blackband SJ, Horsman A. Comparison of conventional single echo and multi-echo sequences with a fast spin-echo sequence for quantitative T_2 mapping: application to the prostate. *J Magn Reson Imaging*. 1996;6(4):603-607.
39. Assländer J, Lattanzi R, Sodickson DK, Cloos MA. Optimized quantification of spin relaxation times in the hybrid state. *Magn Reson Med*. 2019;82(4):1385-1397.
40. Assländer J, Glaser SJ, Hennig J. Pseudo steady-state free precession for MR-fingerprinting. *Magn Reson Med*. 2017;77(3):1151-1161.
41. Shridhar Konar A, Qian E, Geethanath S, et al. Quantitative imaging metrics derived from magnetic resonance fingerprinting using ISMRM/NIST MRI system phantom: an international multi-center repeatability and reproducibility study. *Med Phys*. 2021;48(5):2438–2447.
42. Jiang Y, Ma D, Keenan KE, Stupic KF, Gulani V, Griswold MA. Repeatability of magnetic resonance fingerprinting T_1 and T_2 estimates assessed using the ISMRM/NIST MRI system phantom. *Magn Reson Med*. 2017;78(4):1452-1457.
43. Yarnykh VL. Optimal radiofrequency and gradient spoiling for improved accuracy of T_1 and B_1 measurements using fast steady-state techniques. *Magn Reson Med*. 2010;63(6):1610-1626.
44. Hurley SA, Yarnykh VL, Johnson KM, Field AS, Alexander AL, Samsonov AA. Simultaneous variable flip angle-actual flip angle imaging method for improved accuracy and precision of three-dimensional T_1 and B_1 measurements. *Magn Reson Med*. 2012;68(1):54-64.
45. Kjos BO, Ehman RL, Brant-Zawadzki M, Kelly WM, Norman D, Newton TH. Reproducibility of relaxation times and spin density calculated from routine MR imaging sequences: clinical study of the CNS. *Am J Roentgenol*. 1985;144(6):1165-1170.
46. Noll DC, Meyer CH, Pauly JM, Nishimura DG, Macovski A. A homogeneity correction method for magnetic resonance imaging with time-vaiying gradients. *IEEE Trans Med Imaging*. 1991;10(4):629-637.
47. Kellman P, Bandettini WP, Mancini C, Hammer-Hansen S, Hansen MS, Arai AE. Characterization of myocardial T_1-mapping bias caused by intramyocardial fat in inversion recovery and saturation recovery techniques. *J Cardiovasc Magn Reson*. 2015;17(1):33.
48. Jaubert O, Cruz G, Bustin A, et al. Water–fat Dixon cardiac magnetic resonance fingerprinting. *Magn Reson Med*. 2020;83(6):2107-2123.
49. Ma D, Coppo S, Chen Y, et al. Slice profile and B_1 corrections in 2D magnetic resonance fingerprinting. *Magn Reson Med*. 2017;78(5):1781–1789.
50. Roeloffs V, Uecker M, Frahm J. Joint t_1 and t_2 mapping with tiny dictionaries and subspace-constrained reconstruction. *IEEE Trans Med Imaging*. 2020;39(4):1008-1014.

AUTHOR BIOGRAPHY

Nikolai Mickevicius is a Bentson Translational Research Fellow in the Department of Human Oncology at the University of Wisconsin-Madison. His work focuses on tailored magnetic resonance imaging technology development for challenging problems in radiation therapy.

SUPPORTING INFORMATION

Additional supporting information may be found in the online version of the article at the publisher's website.

How to cite this article: Mickevicius NJ, Kim JP, Zhao J, Morris ZS, Hurst NJ, Glide Hurst CK. Toward magnetic resonance fingerprinting for low-field MR-guided radiation therapy. *Med. Phys.* 2021;1–11. https://doi.org/10.1002/mp.15202